Monitoring the kinetics of the γ' phase in the N18 superalloy using in situ electrical resistivity measurements

Imed-Eddine Benrabah, Gader Altinkurt, Mathieu Fevre, Moukrane Dehmas, Benoit Denand, Frédéric Fossard, Jean Sébastien Mérot, Guillaume Geandier, Didier Locq, Mikael Perrut

Monitoring the kinetics of the γ' phase in the N18 superalloy using *in situ* electrical resistivity measurements

I.-E. Benrabah[a,e,*], G. Altinkurt[a,b], M. Fèvre[b], M. Dehmas[d], B. Denand[a], F. Fossard[b], J.-S. Mérot[b], G. Geandier[a], D. Locq[c], M. Perrut[c]

[a] *Université de Lorraine, IJL, CNRS, Nancy, France*
[b] *Université Paris-Saclay, LEM, CNRS, ONERA, Châtillon, France*
[c] *Université Paris-Saclay, DMAS, ONERA, Châtillon, France*
[d] *Université de Toulouse, CIRIMAT, CNRS, Toulouse, France*
[e] *Université Grenoble Alpes, SIMAP, CNRS, Grenoble INP, Grenoble, France*

Abstract

In nickel-based superalloys, temperatures related to the formation or the dissolution of the different types of γ' precipitates are important parameters for optimizing the mechanical properties of components but also for developing models which can reproduce the kinetics of their phase transformation. We showed that the electrical resistivity variations during heat treatment of the N18 superalloy was sufficient to monitor the kinetics related to secondary and tertiary γ' precipitates. In particular, the effects of the heating rate and the initial microstructure on the dissolution kinetics of the γ' phase were investigated. Experimental results were also compared to outputs of a precipitation model developed for the N18 alloy showing that *in situ* electrical resistivity measurements can be used for calibration and validation purposes.

Keywords: nickel-based superalloys, microstructure, dissolution/precipitation kinetics, electrical resistivity

1. Introduction

Powder metallurgy (PM) nickel-based superalloys are widely used in aeronautics industries especially for high pressure turbine (HPT) disks and compressors. These parts operate at elevated temperatures in oxidizing and corrosive environment under high mechanical stresses. This requires materials with high yield and tensile strength as well as high fatigue and creep resistance. The excellent mechanical properties of Ni based superalloys mainly arise from the hardening of the γ matrix (A1 face centered cubic solid solution) by coherent precipitation of the γ' phase ($L1_2$ ordered cubic structure), but also from the microstruc-

*Corresponding author

tural features, which usually consists in several populations of γ' precipitates, with different sizes, morphologies, volume fractions and, chemical compositions. These features were reported to be strongly dependent on the cooling rate and the aging treatment. Standard solution and aging heat treatments result usually in a trimodal distribution of γ' precipitates, commonly named as primary, secondary and tertiary γ'. Due to chemical and elastic effects, spherical, cubic, octocubic, or plate-like γ' precipitates may be stabilized in the microstructure [1]. A considerable amount of researches has been conducted to correlate the effect of heat treatments and microstructural parameters on fatigue, creep and tensile properties of superalloys (e.g., [2, 3, 4, 5, 6, 7, 8, 9, 10]). The improvement of the microstructure control still occupies an important place in the development of new in Ni-based superalloys with enhanced properties[11, 12, 13].

Understanding the mechanisms governing the dissolution and the precipitation of the γ' in non equilibrium conditions are key steps to predict microstructural changes that can occur when superalloys are in service. For this purpose, kinetics monitoring during different thermal processes is essential.

In many cases, differential thermal analysis (DTA), dilatometry, or electron microscopy observations after interrupted heat treatments were used to monitor the precipitation/dissolution kinetics of the γ' phase (e.g. [14, 15, 16]). The kinetics related to the secondary γ' precipitates was generally well characterized by these techniques as a function of the aging time, and the heating or the cooling rates [17, 18]. However, a little amount of data was obtained for the kinetics related to tertiary γ' precipitates [16, 18]. *Post mortem* characterizations are not very relevant because the microstructure cannot freeze during quenching at room temperature due to the fast kinetics related to these precipitates. Technical restrictions of dilatometry and DTA may also prevent accurate measurements in this case. Indeed, dilatometry is not very sensitive to transformations involving small changes in the atomic volume and low volume fraction variations. In the case of DTA, dissolution and precipitation reactions result in endothermic and exothermic peaks. However, when slow heating and cooling rates are used, peak analysis has been reported to be difficult [9, 10].

The monitoring of the kinetics related to phase transformations can be also realized using electrical resistivity measurements. In titanium alloys, a good correlation was found between the phase transformation kinetics measured with high energy synchrotron X-ray diffraction and the one obtained with this technique [19, 20, 21]. In nickel based superalloys, electrical resistivity measurements were performed for tracking microstructural changes during thermal exposures. Authors reported on technical and analysis developments [22, 23, 24, 25], *in situ* measurements during heating up to 1250 °C [26], isothermal aging [27, 28, 29] and finally, measurements at room temperature after different aging treatments involving long-term exposure [30, 31, 32]. *In situ* measurements were used to study the evolution kinetics of the γ' precipitates during aging [27, 28, 29] and to monitor the evolution of the γ' phase amount during heating in the CMSX4 and Nimonic 901 superalloys [26]. However, the effects of the heating rate on the dissolution kinetics of the γ' phase and on its precipitation during cooling were not investigated by this technique.

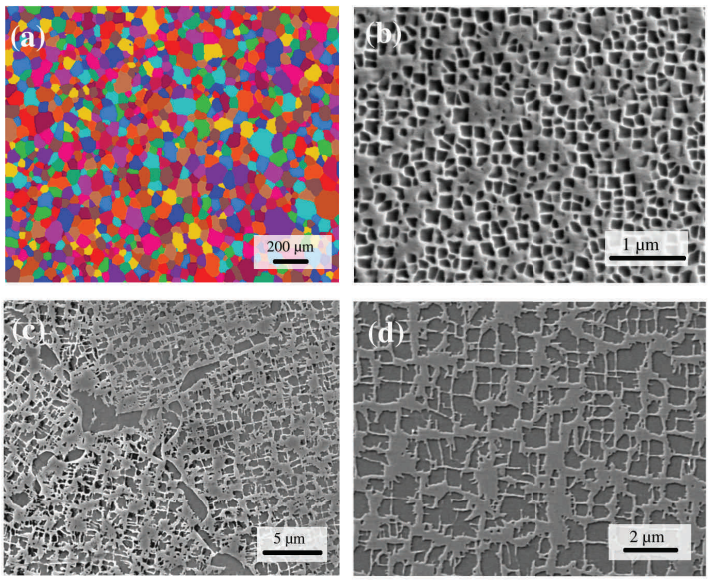

Figure 1: Typical grain and precipitate microstructures of the studied samples. (a) Electron back-scattered diffraction image recorded in a SEM, revealing γ grains (random colors). The average grain size is 40 μm with a distribution ranging from 5 μm to 200 μm. (b) and (d) Secondary electron micrographs showing the microstructures respectively named M1 and M2 in the text. Secondary γ' precipitates correspond to the dark gray color and the γ matrix to the light gray color (see text for detail). (c) micrograph showing intragranular and coarse secondary γ' precipitates located at the grain boundaries in microstructure M2.

The objective of the present study is to show the relevance of electrical resistivity measurements for investigation of dissolution/precipitation kinetics in nickel-based superalloys. To highlight the sensitivity of electrical resistivity measurement, the effects of heating rate and initial microstructure on (i) the dissolution kinetics of the γ' phase, (ii) the temperature ranges corresponding to the dissolution or the precipitation of the secondary and tertiary γ' precipitates were investigated. For the sake of better understanding, the electrical resistivity recorded during heat treatment was also compared to the precipitate volume fraction predicted by a numerical model.

2. Material and methods

Samples were extracted from a HPT disk supplied by Safran Aircraft Engines. The nominal chemical composition of the N18 superalloy was (in weight %) : 16 Co, 11 Cr, 6 Mo, 4 Al, 4 Ti, 0.5 Hf, 0.1 Fe, 0.03 Zr, 0.02 C, 0.2 B, 0.08 O, 0.01 N and balance Ni. Due to a standard sub-solvus heat treatment [33], the as-received microstructure consisted of primary, secondary and tertiary γ' precipitates with a total volume fraction close to 55% and a 10 μm average grain

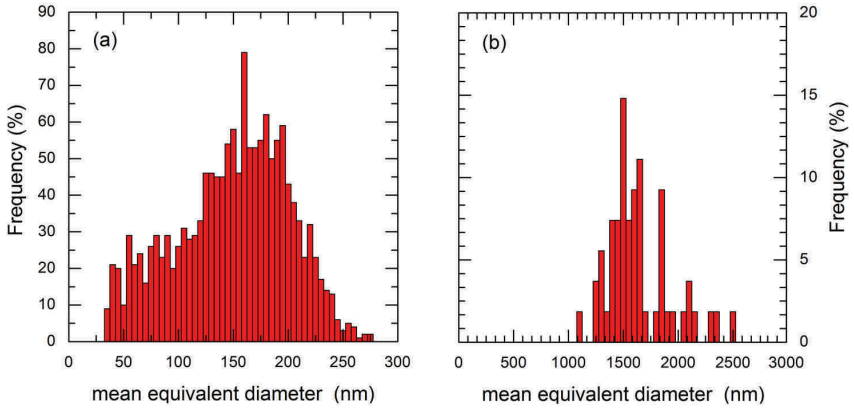

Figure 2: Histograms showing the γ' precipitate size distributions (a) in the M1 microstructure and (b) in the M2 microstructure, obtained from SEM image analysis.

size. To investigate the effect of the precipitate size, two model microstructures were made with an average grain size of 40 μm (Fig. 1a) and only secondary γ' precipitates with sizes close to 200 nm or to 2000 nm (Figs. 1b and 1d). The two microstructures named M1 and M2 thereafter, respectively, were obtained after a supersolvus solution treatment of the as-received material during 4 h at 1205 °C with a 60 °C.min^{-1} heating rate. This temperature was chosen in the solution window whose limits are given by the γ' solvus temperature (1194 °C) and the incipient melting temperature (1227 °C) of the alloy [34]. For M1, the solution treatment was ended by air quenching at room temperature and followed by an aging treatment of 1 h at 900 °C ended by an air quench [7]. For M2, the cooling rate was 7 °C.min^{-1} between 1205 °C and 900 °C followed by air quenching.

After heat treatment of the M1 and M2 samples, the average size of intragranular γ' precipitates and their volume fraction were quantified by the image analysis from images obtained by the secondary electron mode in a ZEISS DSM 962 scanning electron microscope (SEM) operated at 5 kV. The observed samples were prepared by mechanical polishing and chemical etching using a Glyceregia solution containing in volume, 50% HCl, 33% glycerol and 17% HNO_3 [35]. Rietveld refinement using the EMPYREAN X-ray diffractometer (XRD) was employed to determine the volume fraction of the γ' phase. The presence of tertiary γ' precipitates was verified from STEM HAADF and dark field images obtained in a ZEISS LIBRA 200 transmission electron microscope (TEM) operated at 200 kV. The preparation of the thin foils consisted of the mechanical grinding of cylindrical specimen with a diameter of 3 mm down to a thickness of 200 μm. Then, the thin foils were chemically polished at 20 mA and T = 0 °C with a TenuPol-3 double jet electrochemical polisher using an electrolyte containing in volume, 45% acetic acid, 45% 2-butoxyethanol and 10% perchloric

Table 1: Parameters used in the PM N18 superalloy precipitation model to account for the elastic energy caused by the γ' misfitting spherical precipitates in the framework of homogeneous anisotropic elasticity (see Eq. 2). c_{ij} are in the unit of GPa.

c_{11}	c_{12}	s_{1111}	s_{1122}	ϵ_0
239	150	0.448	0.085	-0.3%

acid.

The microstructural evolution of the M1 and M2 samples was monitored during a heat treatment cycle using an in-house built dilatometer which is able to record both the thermal expansion and the electrical resistivity. The temperature of specimen (3 mm × 3 mm × 30 mm bars) was controlled by a lamp furnace associated with gas cooling and was measured by a spot-welded type S thermocouple. The thermal path applied to samples was a heating ramp with a slow ($2\,^{\circ}\mathrm{C.min}^{-1}$) or fast ($60\,^{\circ}\mathrm{C.min}^{-1}$) rate, followed by an isothermal holding at $1205\,^{\circ}\mathrm{C}$ during 1 h, and finally, a cooling ramp down to room temperature at $240\,^{\circ}\mathrm{C.min}^{-1}$. The thermal expansion was determined by linear variable differential transformers. The electrical resistivity was determined with the four-point method where a constant current of 2 A was sent through the sample using two pure platinum wires. The resulting potential difference was then recorded and amplified. To minimize oxidation effects, heat treatments were performed under dynamical vacuum and a pressure between 10^{-4} and 10^{-5} mbar. After the electrical resistivity measurements, the microstructures were observed using a field emission gun FEI Quanta 600 scanning electron microscope operated at 15 kV.

The experimental results were compared to the size and volume fraction evolutions of the different populations of γ' precipitates given by the precipitation model developped for the PM N18 superalloy by Milhet-Gayraud [36, 37] and modified by Boittin [7] and Perrut [38]. This class model implemented in Z-set software [39], relies on a classical nucleation and Lifshitz-Slyozov-Wagner (LSW) coarsening theory. Once the thermal history was provided, the size distribution of intragranular γ' precipitates, thus, the mean size of each class and its volume fraction, were calculated. The grain was assimilated to an infinite medium where precipitates, considered as spheres, do not interact. Heterogeneous nucleation was thus not taken into account. The model was calibrated to reproduce the precipitation of secondary γ' phase during cooling stage for various temperature intervals and rates. The density of elastic energy Δg_{el} caused by the lattice mismatch between the γ matrix and the γ' precipitates can be introduced in the equation that describes the free energy variation ΔG caused by the nucleation of a spherical germ with a radius R:

$$\Delta G = -V(\Delta g_V - \Delta g_{el}) + S\sigma \tag{1}$$

where Δg_V is the free energy difference between the γ' and γ bulk phases (per unit volume), σ the interface energy, $V = \frac{4}{3}\pi R^3$ and $S = 4\pi R^2$ are the precipitate volume and area of spherical precipitate, respectively. Δg_{el} was calculated using the expression reported in Ref. [40]:

$$\Delta g_{el} = \frac{3}{2} f(1-f)(c_{11}+2c_{12})(1-s_{1111}-2s_{1122})\,\epsilon_0^2 \quad (2)$$

$$= f(1-f)\,\Delta\tilde{g}_{el} \quad (3)$$

where c_{ij} are the components of the elastic stiffness tensor of the inclusions, s_{ijkl} the Eshelby tensor components, ϵ_0 the precipitate misfit strain and, f the volume fraction of precipitates. The anisotropic elastic moduli c_{ij} of the γ matrix and the γ' precipitates were assumed identical (homogeneous anisotropic elasticity) and temperature independent. They were calculated using the Eshelby-Kröner approximation, which provides relationships between the macroscopic effective elastic constants of the elastically isotropic material and the elastic constants of the crystallites (see Appendix A). For this purpose, the Young modulus (E = 216 GPa) and the Poisson's ratio ($\nu = 0.3$) of the N18 superalloy measured at room temperature were used in the calculations as well as a Zener anisotropy factor ($A = 2.8$) corresponding to the elastic anisotropy of the AM1 single crystal nickel based superalloy [41]. As the resulting values were close to the elastic moduli of pure nickel, the values of the Eshelby tensor components were taken from the literature [42]. Finally, the misfit strain $\epsilon_0 = (a_{\gamma'} - a_\gamma)/a_\gamma$ was determined from the unstrained lattice parameters a of the γ and γ' phases reported in Ref. [33]. The parameter values used in Eq. 2 are given in Tab. 1.

3. Results and discussion

3.1. Initial microstructures

SEM observations showed that M1 microstructure was characterized by precipitate sizes ranging from 30 nm to 400 nm with an average size of 131(47) nm (Fig.2a) and a 42(3)% volume fraction (Fig. 1b). The standard deviation is given in brackets. Due to the octocubic morphology of precipitates in M2, the determination of an accurate size by automatic image analysis was not possible (Fig. 1d). The manual analysis of about 100 precipitates led to sizes in the 900-2100 nm range (Fig. 2b) with a 37(5)% volume fraction. For both microstructures, coarse secondary γ' precipitates were also observed by SEM at the grain boundaries (Fig. 1c). The volume fraction of the γ' phase determined from XRD measurements for M1 and M2 was found to be 43% and 44% respectively, in good agreement with the values obtained from image analysis. In agreement with the work of Boittin [7], no tertiary γ' precipitates were observed at the SEM scale after heat treatment.

TEM observations were also carried out in samples with M1 or M2 microstructures. As shown in STEM HAADF micrographs (Fig. 3), some γ' precipitates with sizes of few tens of nanometers (< 60 nm) were clearly observed

in different locations in M1, whereas almost no precipitates were visible between the secondary γ' precipitates in M2. Dislocation lines around the octocubic precipitates were clearly observed in the bright field images of M2 (Fig. 3(e)-(f)). In contrast to M1, the presence of these dislocations in M2 is commonly associated with an incoherent interface between γ' precipitates and γ matrix due to their larger size.

3.2. Effect of the heating rate

The evolution of the electrical resistivity (normed by electrical resistivity at room temperature) during heat treatment for the two heating rates of $2\,^{\circ}\mathrm{C.min^{-1}}$ and $60\,^{\circ}\mathrm{C.min^{-1}}$ from microstructure M2 is shown in Fig. 4. For the sake of clarity, the heating, the holding and the cooling stages are shown separately. The general behavior of the electrical resistivity was similar for the two rates: during the heating stage, an increase of the electrical resistivity was observed up to about T = 900 °C, and then, a decrease up to T = 1205°C corresponding to the dissolution of the intragranular secondary γ' precipitates (Fig. 4a). The holding stage was nearly a plateau and the complete dissolution of the γ' phase was assumed to be reached after about 20 min or 40 min depending of the applied heating rate (Fig. 4b). Finally, during the cooling stage, the first increase of the resistivity starting close to T = 1155 °C was related to the precipitation of secondary γ' precipitates. The second increase close to 660 °C was related to the precipitation of tertiary γ' precipitates (Fig. 4c). After heat treatment, the two microstructures were characterized by SEM and both featured secondary and tertiary γ' precipitates with sizes in the 100-400 nm range and lower than 50 nm, respectively (Fig. 5). The volume fraction of the γ' phase was 38% on both cases. Due to a faster cooling rate ($240\,^{\circ}\mathrm{C.min^{-1}}$) in comparison with the one used to make M2 ($7\,^{\circ}\mathrm{C.min^{-1}}$), the amount of coarse γ' precipitates located at the grain boundaries was significantly lower (Fig. 1c and Fig. 5a).

Since no tertiary γ' precipitates were observed by SEM and TEM, the fact that change in slope occurred during the heating stage close to 650 °C (Fig. 4a) tends to show that a phenomenon correlated to the morphology of the secondary γ' precipitates or to the precipitation of tertiary γ' precipitates happened. This point is discussed in the next section. The slope variations that occurred at the end of the heating stage for the slow heating rate (T > 1100 °C) and during the holding stage (t > 5 min) for the fast heating rate (Fig. 4b) were attributed to the dissolution of the coarse γ' precipitates. The double slope variation was probably caused by the combined effects of the dissolution of the γ' phase and the unpinning of the grain boundaries on the electrons motion.

Electrical resistivity measurements reported in Figs. 4a and 4b obviously show that increasing the heating rate from $2\,^{\circ}\mathrm{C.min^{-1}}$ to $60\,^{\circ}\mathrm{C.min^{-1}}$ has a significant effect on the γ' phase dissolution kinetics. The onset temperature of dissolution was indeed shifted by 100 °C for the secondary γ' precipitates and the dissolution of the coarse γ' precipitates located at the grain boundaries mostly happened during heating for the slowest heating rate and during the holding stage for the fastest one. As a consequence, the complete dissolution

of the γ' phase was reached after about 20 min at T = 1205 °C for the former case and after about 40 min for the latter.

The dilatational response was much less sensitive to the dissolution or the precipitation kinetics of the γ' phase than the electrical one. As illustrated in Fig. 6, during the heating stage, only the dissolution of the secondary γ' precipitates modified continuously the coefficient of thermal expansion. The phenomena related to the electrical response variations observed close to T = 600 °C and the dissolution of the coarse γ' precipitates close to T = 1150 °C did not caused a measurable change of thermal expansion coefficient. This was probably due to the small amount of γ' phase involved and to the too small atomic volume variation. The complete or partial character of the dissolution phenomena depending on the heating rate was visible in dilatometry. During the cooling stage, our results were comparable to those already reported by Gayraud *et al.* [36], who monitored the precipitation kinetics by dilatometry. The precipitation of the secondary γ' phase was clearly identified. However, the dimensional variations were not enough to obtain helpful data related to the tertiary γ' precipitates.

3.3. Effect of the precipitate size

The effect of the γ' precipitate size on the dissolution kinetics during heat treatment was investigated for a heating rate of 60 °C.min^{-1}. The electrical resistivity related to M1 and M2 microstructures are both represented in Fig. 7 for the heating and isothermal holding stages only. The dissolution of secondary γ' precipitates with an average size of 200 nm (M1) began 30 °C after the one related to 2000 nm (M2) but with a faster kinetics. This last point can be explained if we consider that, for a given volume fraction of precipitates, a microstructure with small precipitates has more γ-γ' interfaces to promote the diffusion of chemical species than a microstructure with larger precipitates. In contrast, the fact that the onset dissolution temperature was lower for the microstructure with the largest precipitates could not be explained with confidence without further investigations. Diffusion pipelines related to interface dislocations likely contribute to accelerate the dissolution kinetics of the γ' precipitates [43, 44]. The time required to remove the coarse γ' precipitates pinned at the grain boundaries was similar for the two microstructures (about 40 min) even if the dissolution started during the heating stage for the M1 microstructure and during the isothermal holding for the M2 microstructure (Fig. 6b). Finally, the double slope change observed at T = 620 °C and T = 710 °C for M2 was almost absent for M1.

The origin of these slope variations of the electrical resistivity was difficult to explain. In the case of M1 microstructure, the slope could have been modified by the dissolution of fine tertiary precipitates observed in TEM (Figs. 3a,b) if they were considered as stable. However, samples with M1 microstructure were subjected to an aging treatment of 1 hour at 900 °C to remove tertiary precipitates. This means that the small precipitates observed in TEM originated from partial dissolution. Then the growth of tertiary precipitates and their stability occured at a temperature lower than T = 900°C during the heating stage.

In M2, since no tertiary γ' precipitates were observed in SEM and TEM images (Figs. 3b,c), the double slope variation of the electrical resistivity may be caused by a change in the precipitate shape. A similar double variation was also observed in a sample with an average grain size of 62 μm and an average γ' precipitate size of 2000 nm (not shown) indicating that this phenomenon was more related to the intragranular microstructure than to the grain microstructure. It may be also assume that the dislocations observed around the γ' precipitates (Fig. 3f) started to move at a temperature close to T = 600 °C. The release of residual stresses accumulated during air quenching of the samples could also contribute in the change in slope of the electrical resistivity. Finally, precipitation and dissolution of tertiary precipitates during the heating stage may also be an explanation for the slope variations observed close to T = 600 °C. This relies on the fact that M1 and M2 microstructures are expected far from thermodynamic equilibrium due to the fast cooling rates (air quenching). Although the γ' solvus temperatures and the initial microstructures were different, our results obtained for the heating rate of 60 °C.min^{-1} can be compared to the dissolution kinetics monitored by Masoumi *et al.* [16] using the DTA technique in the AD730 superalloy ($T_{sol.}^{N18}$ = 1195 °C, $T_{sol.}^{AD730}$ = 1100 °C). The initial microstructure analyzed by the authors consisted of 26% of 30 nm sized secondary γ', 3% of 8 nm tertiary γ', 8% of 1.4 μm primary γ' precipitates and few amount of MC carbides. When heating at a quite similar rate (65 °C.min^{-1}), temperatures close to T = 615 °C and T = 800 °C were associated with the dissolution of the tertiary and secondary γ' precipitates respectively. This shows that the variations observed in resistivity measurements close to T = 600 °C are potentially compatible with an evolution related to tertiary γ' precipitates.

3.4. Kinetics reproduced by the precipitation model

Table 2: Comparison between the average sizes and the volume fractions of the γ' precipitates obtained by SEM and XRD characterizations and the precipitation model for M1 and M2 microstructures ($\Delta\tilde{g}_{el}$=0 and $\Delta\tilde{g}_{el}$= 37 J.mol^{-1}).

	secondary γ'		tertiary γ'	
	diameter	fraction	diameter	fraction
		M1		
SEM/XRD	131 nm	43%	0	0%
$\Delta\tilde{g}_{el} = 0$	200 nm	49%	0 nm	0%
$\Delta\tilde{g}_{el} = 37$	142 nm	49%	0 nm	0%
		M2		
SEM/XRD	900-2100 nm	37%	0 nm	0 %
$\Delta\tilde{g}_{el} = 0$	1129 nm	46%	122 nm	2%
$\Delta\tilde{g}_{el} = 37$	791 nm	47%	52 nm	1%

To study the dissolution kinetics, the solution and the aging heat treatments

carried out to generate M1 and M2 were first reproduced in the model. A good agreement was obtained for M1 where the average diameters and the volume fractions of the γ' precipitates were close to SEM and XRD measurements (Table 2). The elastic energy term Δg_{el} in Eq. 2 reduced the difference between the measured and the calculated precipitate sizes to 7%. For M2, only the diameter of secondary γ' precipitates was close to the observations when the elastic energy was neglected. The model with and without elastic effects overestimated their volume fraction by 30%. Even if the diameter of secondary γ' precipitates was smaller than in the observations, the best agreement was obtained when elasticity was taken into account. The tertiary precipitates predicted by the model were not present in SEM (Fig. 1) and in TEM (Fig. 3) observations. The discrepancies between the calculations and the measurements mainly arise from the facts that (i) the model neglects the effects of the precipitate morphology and of the incoherent character of interfaces which are important effects when slow cooling rates or large size precipitates are involved; (ii) when the model was developed, only qualitative data about the kinetics of tertiary precipitates were available; (iii) the model was not designed to accurately reproduce the kinetics of microstructures with micrometer size precipitates but rather microstructures with nanometer size precipitates which result in better mechanical properties of superalloys used in HPT disks and compressors.

The precipitation model was fitted by Boittin *et al.* [45] to reproduce the volume fraction and the size of secondary γ' precipitates as well as the presence of tertiary γ' precipitates following different quenching and aging treatments. Good agreements between experimental and calculated quantities were obtained for the M1 and M2 microstructures investigated in this work. Elastic effects described by Eq. 2 were not considered. Thanks to the electrical resistivity measurements, the capability of the model to reproduce the precipitation kinetics during a cooling ramp at $240\,^{\circ}\mathrm{C.min}^{-1}$ from $1205\,^{\circ}\mathrm{C}$ was addressed in this work. Although the undercooling for the nucleation of secondary γ' precipitates was overestimated of $21\,^{\circ}\mathrm{C}$ in the modeling, the behavior of the electrical resistivity and the calculated γ' volume fraction were similar down to the end of precipitation of secondary precipitates close to $850\,^{\circ}\mathrm{C}$ (Fig. 8). The model also correctly predicted the precipitation of tertiary precipitates but with unreliable temperature intervals and precipitate diameters (with and without elastic effects).

The dissolution kinetics of secondary precipitates monitored by electrical resistivity during a heating rate at $60\,^{\circ}\mathrm{C.min}^{-1}$ for M1 microstructure was compared to their calculated volume fraction. The onset temperature of dissolution was underestimated to about $100\,^{\circ}\mathrm{C}$ in the modeling (Fig. 9). This value was weakly affected by elastic effects (about $15\,^{\circ}\mathrm{C}$). Precipitation and dissolution of tertiary γ' precipitates did not occur in the calculations. The dissolution kinetics of M2 is represented in figures 10a and 10b for the heating rates of $2\,^{\circ}\mathrm{C.min}^{-1}$ and $60\,^{\circ}\mathrm{C.min}^{-1}$ respectively. Dashed lines correspond to calculations taking into account the elastic energy term in Eq. 2. For the two rates, calculations showed an increase of the volume fraction related to tertiary precipitates close to $800\,^{\circ}\mathrm{C}$ prior to the dissolution close to $900\,^{\circ}\mathrm{C}$ (black lines). It is

noteworthy that the growth followed by a complete dissolution of quaternary γ' precipitates was predicted, which was emphasized without taking into account the elastic energy. The onset temperatures for the dissolution of secondary γ' precipitates were close to 925 °C and 910 °C for the heating rates of 2 °C.min^{-1} and 60 °C.min^{-1}, respectively. This hierarchy would not have been expected if tertiary precipitates were neglected. The effect of the heating rate was thus less important than in the measurements where a difference of 100 °C was observed. All together, in the calculations, the total volume fraction of the γ' phase started to decrease for the temperatures close to 850 °C (850 °C) and 975 °C (915 °C) for both heating rates, where values in brackets correspond to calculations including elasticity. These values were in relatively good agreement with respect to measurements. This is consistent with the fact that the onset temperature of dissolution is shifted to the high temperatures as the heating rate increases. Diffusion times getting more limited with increasing heating rates, higher temperatures are required to activate the diffusion process. The absence of new dissolution phenomenon for temperatures higher than T = 1000 °C (Figs. 10b and 10c) consolidated the fact that the slope variations observed during the *in situ* electrical resistivity measurements were indeed related to heterogeneous dissolution. Finally, the model also correctly reproduced the partial or complete dissolution of the γ' phase during the heating stage as a function of the heating rate (Fig. 10c).

In brief, the comparison with the *in situ* electrical resistivity measurements showed that the precipitation kinetics of secondary precipitates was correctly described by the model. The precipitation kinetics related to tertiary precipitates was not consistent with measurements. In the case of the dissolution kinetics of secondary γ' precipitates, the best agreement was obtained for the microstructure M2 made of large-sized precipitates for a heating rate of 60 °C.min^{-1}. Good results were also obtained for M2 microstructure upon heating at 2 °C.min^{-1}. This was mainly due to the presence of tertiary precipitates which were not observed in the investigated samples. For M1, the dissolution of secondary precipitates started at about 100 °C before the decrease of the electrical resistivity when heating at 60 °C.min^{-1}. The results of the calculations also suggested that the precipitation of small precipitates, that where not initially present in the microstructure, may have occurred during the heating stage. This consolidated the hypothesis that the slope variations in electrical resistivity observed close to 600 °C were probably due to the precipitation and the dissolution of tertiary γ' precipitates during the heating stage.

4. Conclusions

Electrical resistivity variations from model microstructures of the N18 nickel-based superalloy were sufficient (i) to study *in situ* the kinetics of dissolution of the γ' phase during a heat treatment involving temperatures up to T = 1205 °C and (ii) to highlight heating rates and precipitate size effects. The comparison with the dimensional behavior recorded simultaneously during the heat treatment clearly showed the advantage of electrical resistivity for tracking phase

transformation during the heat treatments. Despite the qualitative analysis of the electrical resistivity measurements due to the complexity of the electronic transport, a wide number of useful data was obtained concerning heating rate and precipitate size effects. Experimental results served to address the outcomes of a semi-analytical precipitation model developed for N18 alloy and to identify possible improvements especially concerning the nucleation and the dissolution of the tertiary γ' precipitates. The main conclusions of this study can be summarized as follows:

- During heating stage, the dissolution kinetics of the γ' phase was controlled by the solute diffusion. The onset temperature of dissolution of the secondary γ' precipitates was shifted by 100 °C when the heating rate was multiplied by a factor of 30.
- Measurements with a heating rate of 2 °C.min^{-1} revealed that the dissolution related to coarse precipitates (secondary γ') pinned at the grain boundaries began 250 °C above the one related to intragranular precipitates. For a heating rate of 60 °C.min^{-1}, the complete dissolution of the γ' phase was obtained after about 45 minutes at T = 1205 °C.
- The most probable cause of the electrical resistivity variations observed close to T = 600 °C was the precipitation and dissolution of tertiary precipitates, which were not initially present in the studied microstructures. This hypothesis was supported by the precipitation calculations. Nevertheless, dislocation motion, and release of residual stresses accumulated during the air quenching were not fully excluded in this work.
- During the 240 °C.min^{-1} cooling stage, the electrical resistivity was an excellent tracer to monitor the precipitation kinetics of secondary and tertiary phases.
- Even if the volume fractions were not determined experimentally, the comparison of the electrical resistivity with the volume fraction evolution calculated with the N18 precipitation model showed a similar behavior. A relatively good agreement for the precipitation and dissolution temperatures related to the intragranular secondary γ' precipitates was obtained, especially in the microstructure with large size precipitates. The discrepancies observed for the tertiary precipitates were reduced in the model by introducing elastic effects arising from the lattice strain between the γ and the γ' phases. This study also highlighted the need to improve the model calibration both in the precipitation and the dissolution regimes to better account for kinetics concerns.

Finally, this study outlined the useful contribution of *in situ* electrical resistance measurements for monitoring the diffusion phenomena involved during precipation or the dissolution of the different types of γ' precipitates in nickel based superalloys. It also showed the need to develop physically justified models in which electrical transport is included in addition to chemical and elastic effects for quantitative analysis purposes.

Acknowledgments

This work benefited from the support of the REMEDDIES project (ANR-13-BS09-016) of the French National Research Agency (ANR) and the French Aeronautical and Space Research Foundation (FRAE). Authors gratefully acknowledge C. Ramusat and D. Boivin for the SEM characterizations.

Appendix A. Derivation of the cubic crystal elastic moduli from the effective isotropic elastic constants of the related polycrystal

The two macroscopic elastic moduli of a perfectly disordered material were derived by Voigt, Reuss and Kröner from the anisotropic elastic moduli of the crystallites. Within the Kröner approximation and for cubic crystals with elastic moduli c_{ij}, the Young modulus E^K and the Poisson's ratio ν^K are given by the following expressions:

$$E^K = \frac{9KG}{3K+G} \quad ; \quad \nu^K = \frac{3K-2G}{6K+2G} \tag{A.1}$$

where K=$(c_{11}+2c_{12})/3$ and G is the solution of the following polynomial equation:

$$G^3 + \frac{1}{8}(9K+4\nu')\,G^2 - \frac{1}{8}(3K+12\nu')\mu\,G - \frac{3}{4}K\mu\nu' = 0 \tag{A.2}$$

with ν'=$(c_{11}-c_{12})/2$ and $\mu = c_{44}$. The Zener anisotropy factor A of the crystal being given by $2c_{44}/(c_{11}-c_{12})$=μ/ν', the elastic moduli c_{ij} can be thus calculated from the values of E^K, ν^K and A. After simple maths, the elastic moduli c_{ij} of the cubic crystal are given by :

$$c_{11}^{\pm} = \frac{3K+4\nu'^{\pm}}{3}\,;\, c_{12}^{\pm} = \frac{3K-2\nu'^{\pm}}{3}\,;\, c_{44}^{\pm} = A\nu'^{\pm} \tag{A.3}$$

where ν' is the solution of a second order equation :

$$\nu'^{\pm} = \frac{-b \pm \sqrt{b^2-4ac}}{2a} \text{ with } \left\{ \begin{array}{l} a = 6(K+2G)A \\ b = 4(G-3KA)G\,, \\ c = (8G+9K)G^2 \end{array} \right. \tag{A.4}$$

, with $2G = E^K/(1+\nu^K)$ and $3K = E^K/(1-2\nu^K)$. For $E^K = 216$ GPa, $\nu^K = 0.3$ and $A = 2.8$, Eq. A.4 yields $c_{11} = 239$ GPa, $c_{12} = 150$ GPa and $c_{44} = 124$ GPa.

References

References

[1] T. Grosdidier, A. Hazotte, A. Simon, Precipitation and dissolution processes in γ/γ' single crystal nickel-based superalloys, Materials Science and

Engineering: A 256 (1) (1998) 183 – 196. doi:https://doi.org/10.1016/S0921-5093(98)00795-3.

[2] P. R. Bhowal, E. F. Wright, E. L. Raymond, Effects of cooling rate and γ' morphology on creep and stress-rupture properties of a powder metallurgy superalloy, Metallurgical Transactions A 21 (6) (1990) 1709–1717. doi:10.1007/BF02672587.

[3] H. Pang, P. Reed, Effects of microstructure on room temperature fatigue crack initiation and short crack propagation in Udimet 720Li Ni-base superalloy, International Journal of Fatigue 30 (10) (2008) 2009 – 2020. doi:https://doi.org/10.1016/j.ijfatigue.2008.01.001.

[4] T. P. Gabb, J. P. Gayda, J. Telesman, A. Garg, O. Cleveland, The effects of heat treatment and microstructure variations on disk superalloy properties at high temperature, Proceedings of the International Symposium on Superalloys (2008) 121–130doi:https://doi.org/10.7449/2008/Superalloys_2008_121_130.

[5] J.-R. Vaunois, J. Cormier, P. Villechaise, A. Devaux, B. Flageolet, Influence of both γ' distribution and grain size on the tensile properties of udimet 720Li at room temperature, Proceedings of the International Symposium on Superalloys (2010) 199–213.

[6] J. Cormier, G. Cailletaud, Constitutive modeling of the creep behavior of single crystal superalloys under non-isothermal conditions inducing phase transformations, Materials Science and Engineering: A 527 (23) (2010) 6300 – 6312. doi:https://doi.org/10.1016/j.msea.2010.06.023.

[7] G. Boittin, D. Locq, A. Rafray, P. Caron, P. Kanouté, F. Gallerneau, G. Cailletaud, Influence of γ' precipitate size and distribution on LCF behavior of a PM disk superalloy, Proceedings of the International Symposium on Superalloys (2012) 167–176doi:10.1002/9781118516430.ch19.

[8] K. Maciejewski, H. Ghonem, Influence of continuum precipitates on intergranular fatigue crack growth of a P/M nickel-based superalloy, Materials Science and Engineering: A 560 (2013) 439 – 449. doi:https://doi.org/10.1016/j.msea.2012.09.088.

[9] J.-B. le Graverend, J. Cormier, F. Gallerneau, P. Villechaise, S. Kruch, J. Mendez, A microstructure-sensitive constitutive modeling of the inelastic behavior of single crystal nickel-based superalloys at very high temperature, International Journal of Plasticity 59 (2014) 55 – 83. doi:https://doi.org/10.1016/j.ijplas.2014.03.004.

[10] T. Sugui, T. Ning, Y. Huichen, M. Xianlin, L. Ying, Influence of solution temperature on microstructure and creep property of a directional solidified nickel-based superalloy at intermediate temperatures, Materials Science and Engineering: A 615 (2014) 469 – 480. doi:https://doi.org/10.1016/j.msea.2014.07.103.

[11] X. Zhang, H. Li, M. Zhan, Mechanism for the macro and micro behaviors of the Ni-based superalloy during electrically-assisted tension: Local joule heating effect, Journal of Alloys and Compounds 742 (2018) 480 – 489. doi:https://doi.org/10.1016/j.jallcom.2018.01.325.

[12] Y. Wu, Y. Liu, C. Li, X. Xia, J. Wu, H. Li, Coarsening behavior of γ' precipitates in the γ+γ'area of a Ni_3Al-based alloy, Journal of Alloys and Compounds 771 (2019) 526 – 533. doi:https://doi.org/10.1016/j.jallcom.2018.08.265.

[13] J. Wu, C. Li, Y. Liu, Y. Wu, Q. Guo, H. Li, H. Wang, Effect of annealing treatment on microstructure evolution and creep behavior of a multiphase Ni_3Al-based superalloy, Materials Science and Engineering: A 743 (2019) 623 – 635. doi:https://doi.org/10.1016/j.msea.2018.11.126.

[14] N. Gayraud, F. Moret, Y. Desvalley, Etude expérimentale et simulation numérique de la cinétique de précipitation de l'evolution microstructurale dans le superalliage N18 au cours de la trempe, J. Phys. IV 05 (C3) (1995) C3–225–C3–235. doi:10.1051/jp4:1995320.

[15] M. Soucail, Y. Bienvenu, Dissolution of the γ' phase in a nickel base superalloy at equilibrium and under rapid heating, Materials Science and Engineering: A 220 (1) (1996) 215 – 222. doi:https://doi.org/10.1016/S0921-5093(97)80011-1.

[16] F. Masoumi, M. Jahazi, D. Shahriari, J. Cormier, Coarsening and dissolution of γ' precipitates during solution treatment of AD730 ni-based superalloy: Mechanisms and kinetics models, Journal of Alloys and Compounds 658 (2016) 981 – 995. doi:10.1016/j.jallcom.2015.11.002.

[17] R. Radis, M. Schaffer, M. Albu, G. Kothleitner, P. Pölt, E. Kozeschnik, Evolution of size and morphology of γ' precipitates in Udimet 720 Li during continuous cooling, Proceedings of the International Symposium on Superalloys (2008) 829–836.

[18] A. Singh, S. Nag, S. Chattopadhyay, Y. Ren, J. Tiley, G. Viswanathan, H. Fraser, R. Banerjee, Mechanisms related to different generations of γ' precipitation during continuous cooling of a nickel base superalloy, Acta Materialia 61 (1) (2013) 280 – 293. doi:https://doi.org/10.1016/j.actamat.2012.09.058.

[19] F. Bruneseaux, E. Aeby-Gautier, G. Geandier, J. D. C. Teixeira, B. Appolaire, P. Weisbecker, A. Mauro, *In situ* characterizations of phase transformations kinetics in the Ti17 titanium alloy by electrical resistivity and high temperature synchrotron x-ray diffraction, Materials Science and Engineering: A 476 (1) (2008) 60 – 68. doi:https://doi.org/10.1016/j.msea.2007.04.072.

[20] A. Settefrati, E. Aeby-Gautier, M. Dehmas, G. Geandier, B. Appolaire, S. Audion, J. Delfosse, Precipitation in a near beta titanium alloy on ageing: Influence of heating rate and chemical composition of the beta-metastable phase, in: Solid-Solid Phase Transformations in Inorganic Materials, Vol. 172 of Solid State Phenomena, Trans Tech Publications, 2011, pp. 760–765. doi:10.4028/www.scientific.net/SSP.172-174.760.

[21] A. Settefrati, Etude expérimentale et modélisation par champ de phase de la formation de α dans les alliages de titane β-métastable, Ph.D. thesis, Université de Lorraine (2012).
URL http://www.theses.fr/2012LORR0092

[22] K. D. Maglić, N. L. Perović, A. M. Stanimirović, Calorimetric and transport properties of Zircalloy 2, Zircalloy 4, and Inconel 625, International Journal of Thermophysics 15 (4) (1994) 741–755. doi:10.1007/BF01563797.

[23] G. Pottlacher, H. Hosaeus, E. Kaschnitz, A. Seifter, Thermophysical properties of solid and liquid Inconel 718 alloy, Scandinavian Journal of Metallurgy 31 (3) 161–168. doi:10.1034/j.1600-0692.2002.310301.x.

[24] D. Basak, R. A. Overfelt, D. Wang, Measurement of specific heat capacity and electrical resistivity of industrial alloys using pulse heating techniques, International Journal of Thermophysics 24 (6) (2003) 1721–1733. doi:10.1023/B:IJOT.0000004101.88449.86.

[25] E. Madhi, P. B. Nagy, In-Situ Resistivity Monitoring of Microstructure Evolution in IN718 Nickel-Base Superalloy, in: D. O. Thompson, D. E. Chimenti (Eds.), American Institute of Physics Conference Series, Vol. 1096 of American Institute of Physics Conference Series, 2009, pp. 1209–1215. doi:10.1063/1.3114092.

[26] B. Roebuck, D. Cox, R. Reed, The temperature dependence of γ' volume fraction in a Ni-based single crystal superalloy from resistivity measurements, Scripta Materialia 44 (6) (2001) 917 – 921. doi:https://doi.org/10.1016/S1359-6462(00)00662-X.

[27] R. White, S. Fisher, K. Miller, G. Swallow, A resistometric study of ageing in nimonic alloys (i). PE16, Journal of Nuclear Materials 52 (1) (1974) 51 – 58. doi:https://doi.org/10.1016/0022-3115(74)90024-5.

[28] R. White, G. Swallow, S. Fisher, K. Miller, A resistometric study of ageing in nimonic alloys (ii). 80a, Journal of Nuclear Materials 55 (3) (1975) 273 – 278. doi:https://doi.org/10.1016/0022-3115(75)90067-7.

[29] G. Rosen, S. Dirnfeld, M. Bamberger, B. Prinz, *In-situ* electrical resistivity measurements for determining formation kinetics of γ' phase in nickel-based wrought superalloys, Zeitschrift Für Metallkunde 85 (1994) 127–130.

[30] R. L. Whelchel, Characterization of a nickel-based superalloy through electrical resistivitymicrostructure relationships facilitated by small angle scattering relationships facilitated by small angle scattering, Master's thesis, Georgia Institute of Technology (2011).

[31] V. S. K. G. Kelekanjeri, R. A. Gerhardt, Etch pit and γ' precipitate evolution in controlled Waspaloy microstructures aged at 725, 800 and 875°C, Acta Materialia 57 (2) (2009) 616 – 627. doi:https://doi.org/10.1016/j.actamat.2008.10.010.

[32] V. S. K. G. Kelekanjeri, L. K. Moss, R. A. Gerhardt, J. Ilavsky, Quantification of the coarsening kinetics of γ' precipitates in Waspaloy microstructures with different prior homogenizing treatments, Acta Materialia 57 (16) (2009) 4658 – 4670. doi:https://doi.org/10.1016/j.actamat.2009.06.019.

[33] S. Wlodek, M. Kelly, D. Alden, The strucuture of N18, Proceedings of the International Symposium on Superalloys (1992).

[34] J.-Y. Guédou, I. Augustins-Lecallier, L. Nazé, P. Caron, D. Locq, Development of a new fatigue and creep resistant PM nickel-base superalloy for disk applications, Proceedings of the International Symposium on Superalloys (2008) 21–30doi:10.7449/2008/Superalloys_2008_21_30.

[35] G. Vander Voort, E. Manilova, Metallographic techniques for superalloys, Microscopy and Microanalysis 10 (S02) (2004) 690–691. doi:10.1017/S1431927604883442.

[36] N. Gayraud, E. Moret, X. Baillin, P. E. Mosser, Precipitation kinetics in N18 P/M superalloy: Experimental study and numerical modelling, Journal De Physique IV 03 (1993) 271–276.

[37] N. Milhet-Gayraud, Etude expérimentale et modélisation de la précipitation γ' dans le superalliage, Ph.D. thesis, thèse de doctorat dirigée par Louchet, François Science et Génie des matériaux Grenoble INPG 1994 (1994).
URL http://www.theses.fr/1994INPG0035

[38] M. Perrut, D. Locq, Precipitation kinetics in the powder metallurgy superalloy N19 and influence of the precipitation latent heat, MATEC Web of Conferences 14 (2014) 09004. doi:10.1051/matecconf/20141409004.

[39] Z-set / zébulon, material and structure analysis suite (2011).
URL http://www.zset-software.com/

[40] N. Ratel, P. Bastie, T. Mori, P. Withers, Application of anisotropic inclusion theory to the energy evaluation for the matrix channel deformation and rafting geometry of γ-γ' Ni superalloys, Materials Science and Engineering: A 505 (1) (2009) 41 – 47. doi:10.1016/j.msea.2008.10.050.

[41] L. Espié, Étude expérimentale et modélisation numérique du comportement de monocristaux de superalliages, Ph.D. thesis, ENSMP (1996).

[42] C.-R. Chiang, Thermal mismatch stress of a spherical inclusion in a cubic crystal, International Journal of Fracture 139 (2) (2006) 313–317. doi:10.1007/s10704-006-8377-2.

[43] R. Giraud, Z. Hervier, J. Cormier, G. Saint-Martin, F. Hamon, X. Milhet, J. Mendez, Strain effect on the γ' dissolution at high temperatures of a nickel-based single crystal superalloy, Metallurgical and Materials Transactions A 44 (2012) 131–146. doi:10.1007/s11661-012-1397-9.

[44] P. Kontis, Z. Li, D. M. Collins, J. Cormier, D. Raabe, B. Gault, The effect of chromium and cobalt segregation at dislocations on nickel-based superalloys, Scripta Materialia 145 (2018) 76 – 80. doi:https://doi.org/10.1016/j.scriptamat.2017.10.005.

[45] G. Boittin, Expérimentation numérique pour l'aide à la spécification de la microstructure et des propriétés en fatigue des superalliages base Ni pour des applications moteur, Ph.D. thesis, Ecole des Mines de Paris (12 2011).

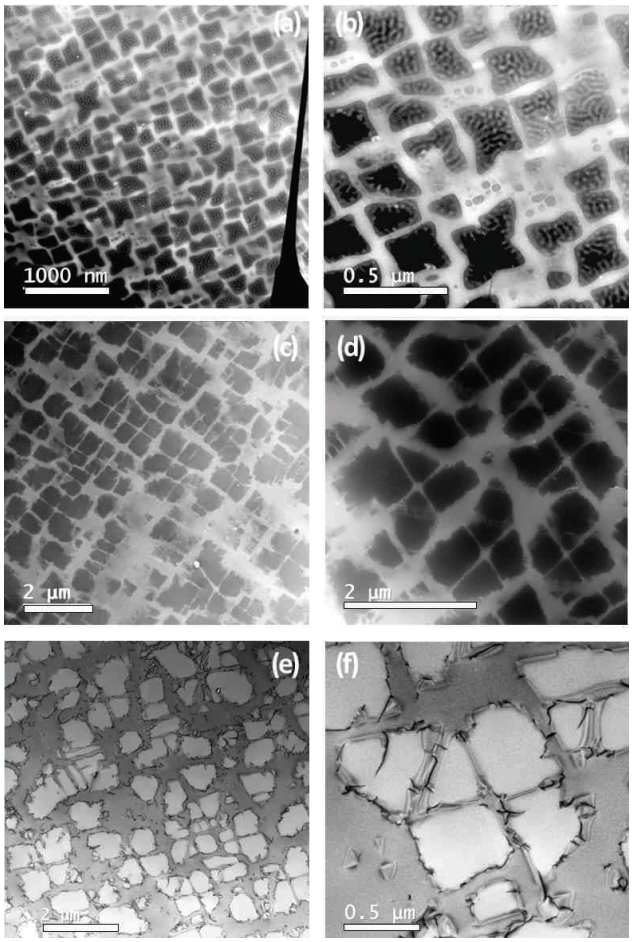

Figure 3: STEM HAADF images of (a)-(b) M1 and (c)-(d) M2 microstructures. The γ' phase correspond to the dark gray and the γ matrix to the light gray. The contrast observed in secondary γ' precipitates in (a) and (b) is attributed to thickness variation (rippling) caused by the electrochemical polishing. (e)-(f) correspond to bright field images of M2 showing dislocation lines at the interfaces between the γ matrix and the γ' precipitates.

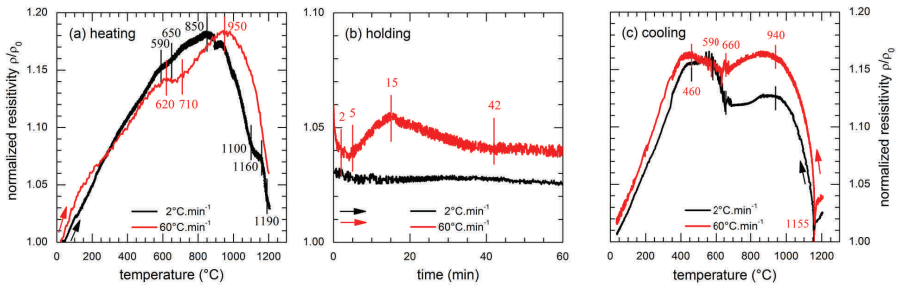

Figure 4: Electrical resistivity recorded during heat treatments from M2 initial microstructure : (a) heating at two rates ($2\,^{\circ}\mathrm{C.min^{-1}}$ and $60\,^{\circ}\mathrm{C.min^{-1}}$), (b) isothermal holding of 1 h at $1205\,^{\circ}\mathrm{C}$ and (c) cooling stage at a rate of $240\,^{\circ}\mathrm{C.min^{-1}}$. Vertical bars indicate the values related to changes in curve slope.

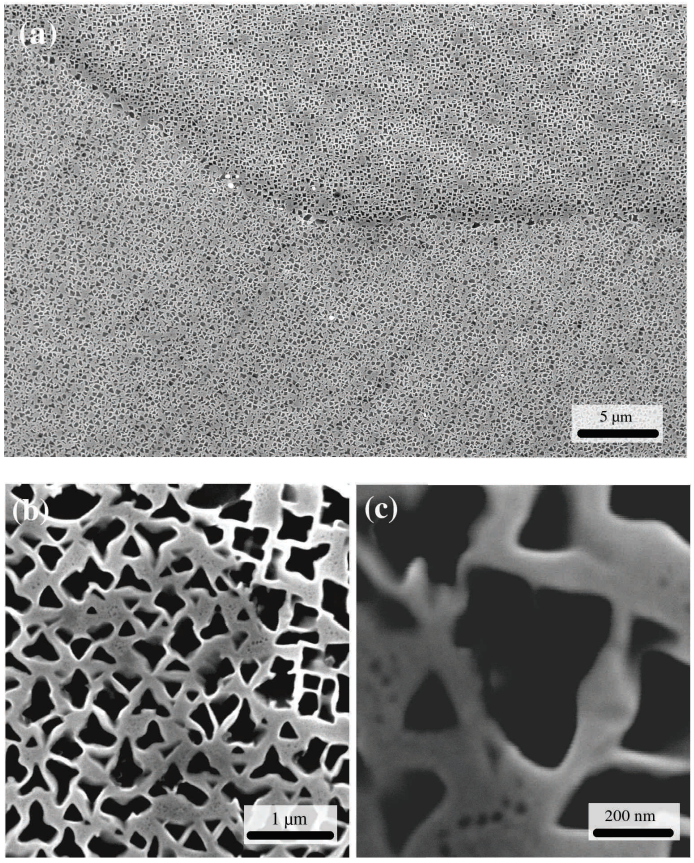

Figure 5: SEM observations of the microstructure obtained at the end of the heat treatment carried out during electrical resistivity measurements of M2 sample. Dark gray corresponds to the γ' phase and light gray to the γ matrix. (a) microstructure close to a grain boundary. (b) and (c) micrographs showing a bimodal size distribution of the γ' precipitates embedded in the γ matrix.

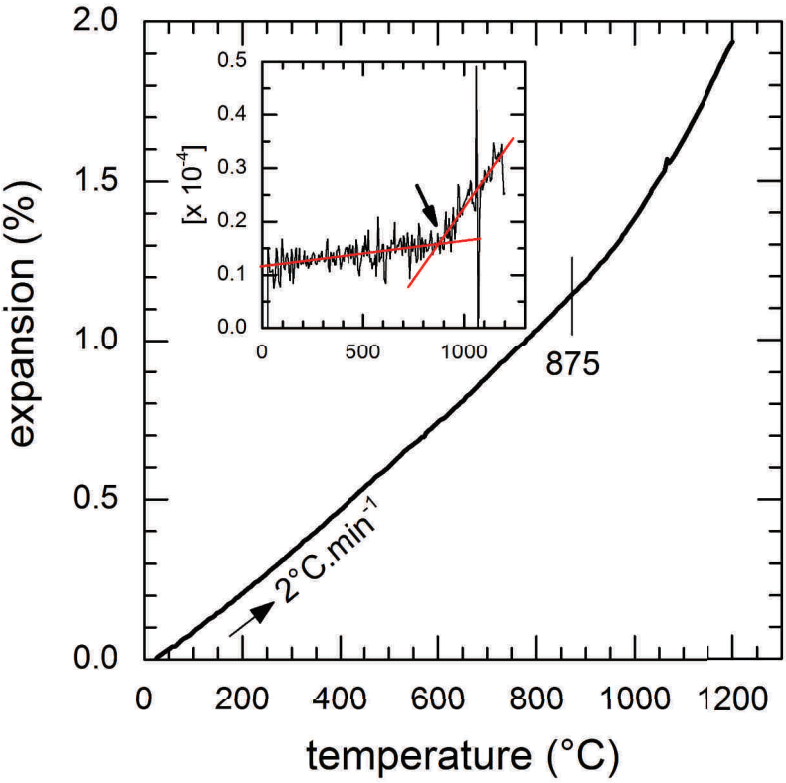

Figure 6: Dimensional behavior recorded the during a heating stage of $2\,^{\circ}\mathrm{C.min}^{-1}$ for the M2 microstructure. The inset corresponds to the first derivative in units of 10^{-4} as a function of the temperature. Red lines are guidelines.

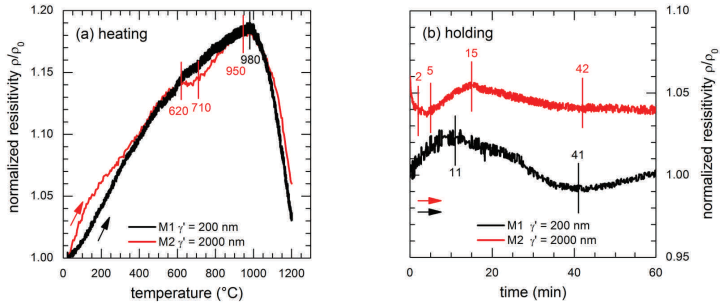

Figure 7: Electrical resistivity recorded in samples with M1 and M2 microstructures during (a) a heating stage with a rate of $60\,^{\circ}\mathrm{C.min}^{-1}$ and (b) an isothermal holding stage at 1205 °C. Vertical bars indicate the values related to specific locations commented in the text.

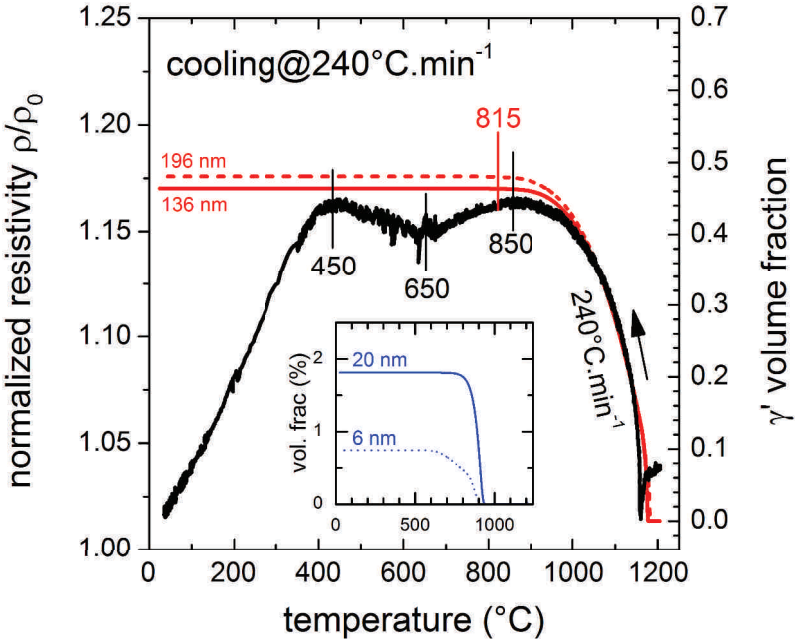

Figure 8: Electrical resistivity (black line and left axis) during the cooling stage at 240 °C.min^{-1} from 1205 °C and secondary γ' volume fraction (red line and right axis) calculated with the N18 precipitation model. Dashed lines refer to calculations with elastic effects and solid lines to calculations without elastic effects. Numbers indicate the diameter of the precipitates. Vertical bars indicate the values related to specific locations commented in the text. The inset correspond to the evolution of the volume fraction of tertiary γ' precipitates and the numbers indicate their diameter.

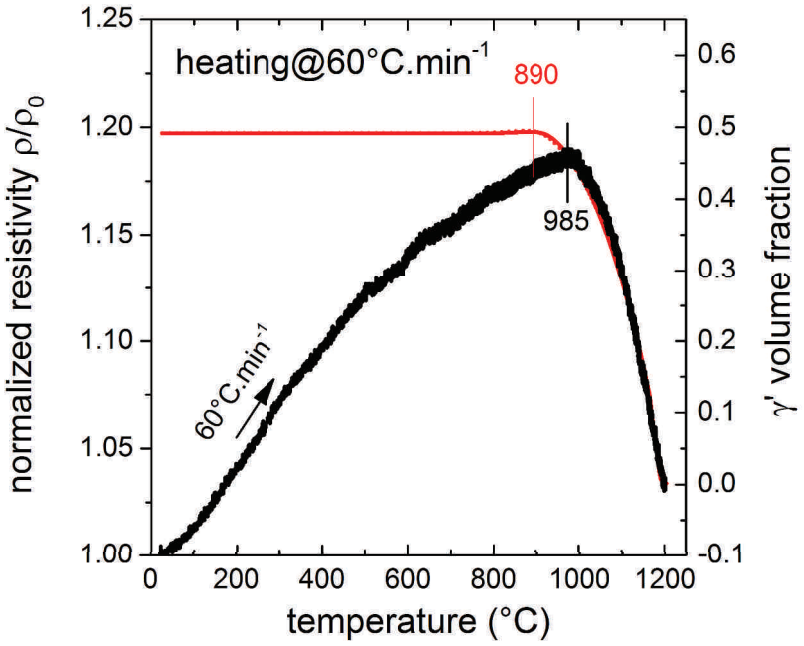

Figure 9: Electrical resistivity (black line and left axis) of M1 during a heating at 60 °C.min^{-1} and, secondary γ' precipitates volume fraction (red line and right axis) calculated with the N18 precipitation model. Vertical bars indicate the values related to specific locations commented in the text.

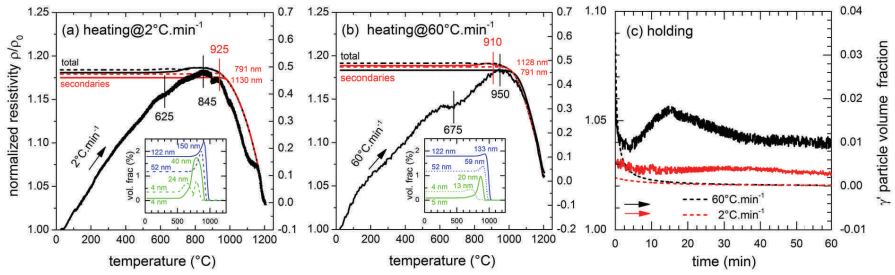

Figure 10: Electrical resistivity (left axes) of M2 during the heating and the holding stages of a thermal cycle up to 1205 °C and γ' precipitates volume fractions (right axes) calculated with the N18 precipitation model. Dashed lines refer to calculations with elastic effects, solid lines to calculations without elastic effects. Insets in figures (a) and (b) correspond to the evolution of the volume fraction of tertiary and quaternary γ' precipitates and the numbers indicate their diameter. The heating rates are 2 °C.min^{-1} in (a) and 60 °C.min^{-1} in (b). Vertical bars indicate the values related to specific locations commented in the text.